Journal of Solid State Chemistry 256 (2017) 101–108

Contents lists available at ScienceDirect

Journal of Solid State Chemistry

journal homepage: www.elsevier.com/locate/jssc

Thermoelectric properties of 2H-$CuGaO_2$ for device applications: A first principle TB-mBJ potential study

K.C. Bhamu[a,*], C.S. Praveen[b]

[a] Dept. of Physics, Goa University, Goa 403206, India
[b] Department of Chemistry and Applied Biosciences, ETH Zurich, Vladimir Prelog Weg 1-5, 8093 Zurich, Switzerland

ARTICLE INFO

Keywords:
A. Semiconductors
B. Optical properties
D. Dielectric properties
D. Electronic structure
D. Thermal conductivity

ABSTRACT

Here we report the structural, electronic, optical, and thermoelectric properties of delafossite type 2H-$CuGaO_2$ using first principles calculations. The present calculation predict an indirect band gap of 1.20 eV and a direct band gap of 3.48 eV. A detailed analysis of the electronic structure is provided based on atom and orbital projected density of states. Frequency dependent dielectric functions, refractive index, and absorption coefficient as a function of photon energy are discussed. The thermoelectric properties with power factor, and the figure of merit are reported as a function of chemical potential in the region $\pm 0.195\ (\mu - E_F)$ eV at constant temperature of 300 and 800 K. The thermoelectric properties shows that 2H-$CuGaO_2$ could be potential candidate for engineering devises operating at high temperature for the chemical potential in the range of $\pm 0.055\ (\mu - E_F)$eV and beyond this range the thermoelectric performance of 2H-$CuGaO_2$ get reduced.

1. Introduction

Transparent conducting oxides (TCOs) have gained much interest in the recent years due to their applications in the emerging field of optoelectronics. For instance, TCOs are widely used in flat panel displays, photovoltaics, touch panels, stacked solar cells, transparent electrodes, etc., depending on the type of conductivity of the used material [1–7]. Commonly used binary oxides such as ZnO, CdO, SnO_2 and In_2O_3:Sn or In_2O_3:Mo, Cu_2O play a significant role in transparent electronics as transparent electrodes [8–13]. However most of these materials are n-type semiconductors and the top of their valence band is composed solely of oxygen 2*p* state due to ionic bonding with the metal cation. This ionic bonding localizes the induced hole charge carriers at the valence band maximum (VBM) resulting in n-type conductivity [14–18]. The n-type conductivity and low hole carrier mobility inhibit their use in p-n semiconductor devices [19,20]. Therefore, to achieve a p-type conductivity in oxide semiconductors, one has to delocalize the bands at the top of the valence band through hybridization of O − 2*p* levels with the cation, preferably a transition metal (TM) atom [6].

The discovery of p-type ternary TCO ($CuAlO_2$) by Kawazoe et al. [1] was a breakthrough in the field of transparent electronics and several experimental [4,6,21–25] and theoretical data [16,26–29] have been reported thereafter. The strong hybridization between *d* state of the TM and the O − 2*p* orbitals near VBM delocalizes the bands, which in turn increase the hole-charge mobility in the valence band. This scenario results in p-type conductivity in TCOs. Generally, in $A^IB^{III}O_2$ type ternary TCOs (referred as delafossites), either Cu or Ag is widely used as an A type cation. However, due to abundance, non-toxicity, low cost, and easy fabrication make Cu a first choice for the A site cation [11,30]. In addition to the widely used $CuAlO_2$, $CuXO_2$ (X=Ga, In) also have reported to exhibit excellent p-type conductivity, despite their anomalous behavior in the band gap [26]. Recently, $CuGaO_2$ has gained much attention as a promising p-type semiconductor due to its high stability against photo corrosion, relatively higher conductivity, and higher transparency in visible region of the solar spectrum [31,32].

Unlike the binary Cu_2O p-type semiconductor, in ternary delafossites, the three-dimensional crosslinking of Cu^+ network is reduced to two-dimensional, though the local symmetry around Cu^+ and O^{2-} remain the same [1,11]. In ternary $CuGaO_2$, the crystal structure can be viewed as a stacking sequence of Ga-O layer. The Ga-O coordination stabilizes the crystal with a Ga-centered, edge-shared octahedral coordination in the *ab* plane, which separates the CuO_2 dumbbell structure along the c axis. Depending on the stacking of this dumbbell-like structure along c-axis, the crystal structure of these type of materials could fall in either $R-3m(3R-)$ or $P63/mmc(2H-)$ space group.

It has been reported [14] that the difference in the formation energy of 2H- and 3R- polymorphs of $CuGaO_2$ is only 0.6 meV. Therefore, $CuGaO_2$ could stabilize in either 2H- or 3R- form, or even an alloy of

* Corresponding author.
E-mail address: kcbhamu85@gmail.com (K.C. Bhamu).

http://dx.doi.org/10.1016/j.jssc.2017.08.008
Received 24 May 2017; Received in revised form 4 August 2017; Accepted 7 August 2017
Available online 15 August 2017

both. Recently, Liu et al. [33] have reported 2H-polymorphs to be mechanically stable, which supports the argument of the stability of the 2H- phase. Several theoretical reports on the structural [34–41] electronic and optical [2,8,14,16,27,28,35–45,32], mechanical [28,33], and thermoelectric [17,18,27,29,34,41,32,46,47] properties of 3R-$CuGaO_2$ have been reported while only few reports are available on 2H-$CuGaO_2$ [29,33,35,48]. Notably, there are no attempt to synthesize the 2H polymorph of $CuGaO_2$ have reported so far although the phase is predicted to be stable. Computational data available on the 2H phase is limited to electronic properties and are mainly based on LDA [29], GGA [33,35], and Hartree-Fock (HF) [48] level of theory. Therefore, the reported band gaps are assessed to be largely overestimated or underestimated. Some recent reports [11,49,50] using Tran-Blahas modified Becke-Johnson potential (TB-mBJ) [51] approach on delafossite type structure indicate that the band gaps obtained using mBJ potential are in very good agreement with the experimentally reported band gaps. It is worth mentioning that, computationally inexpensive TB-mBJ scheme has been reported to be very accurate in predicting band gap value as good as latest hybrid functional or even GW approximation [11,49,50]. Therefore, in this paper, we report the structural, electronic and optical properties of 2H-structure type CuGaO2 using the density functional theory within the framework of mBJ potential. In addition, we have also investigated the thermoelectric properties, which is beneficial for power generation and refrigeration. To the best of the authors knowledge there are no detailed reports on the optoelectronic and transport properties of 2H- phase of $CuGaO_2$.

2. Computational details

All DFT calculations presented in this work employed a full potential linearized augmented plane wave (FP-LAPW) method as implemented in the Wien2K code [52]. The electron exchange and correlation were treated by the generalized gradient approximation (GGA) using the parameterization of Perdew, Burke, and Ernzerh (PBE) [53] and mBJ potential. The energy cut-off parameter was set to −7.2 eV to separate out the core states and valence states. The 2H-phase of delafossite $CuGaO_2$ falls in the *P*63/*mmc* space group, with two formula units per cell. A schematic representation of the unit cell used in the present calculation is reported in Fig. 1.

Lattice parameters and the atomic positions of 2H-$CuGaO_2$ were optimized by minimizing the forces on each atomic site to be less than 0.05 mRy au^{-1}. The convergence in total energy and charge were set to 10^{-5} Ry, and 2×10^{-4} |e| respectively. The integrals over the irreducible Brillouin zone were performed on a (16 × 16 × 3) uniformly shifted Monkhorst-Pack k-point mesh, resulting in 1000k-points, for self-consistency calculations. A very fine k-mesh with 2000k-points in the full BZ (FBZ) were used for calculating the density of states (DOS), and optical properties. The band structure is plotted along the $\Gamma - M - K - \Gamma - A - L - H - A$ high symmetric directions by taking 50 k-points in each direction. Thermoelectric properties were computed using the semiclassical Boltzmann transport theory within the constant relaxation time approximation τ (i.e., assuming directional independence of relaxation time), and the rigid band approach as implemented in BoltzTraP code [54–56], which has proven to be very efficient. For calculating the thermoelectric properties, a much denser mesh with 99,999k-points was used.

3. Results and discussion

3.1. Structural properties

First of all, we have optimized the lattice parameters of $CuGaO_2$ by fitting the Energy vs Volume curve to the 3^{rd} order Brich-Murnaghan equation of state (c.f Eq. (1));

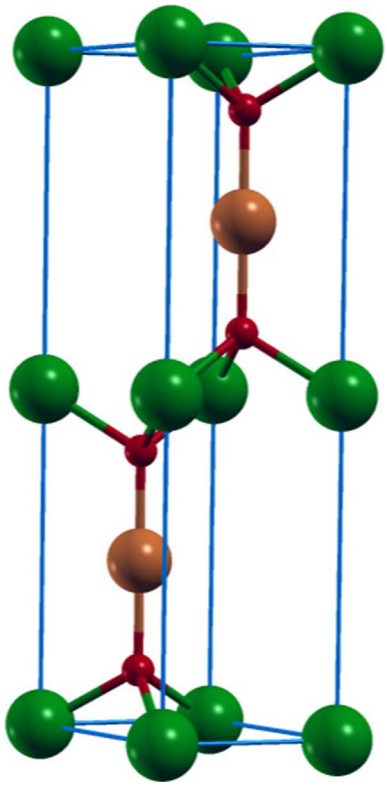

Fig. 1. A pictorial representation of the unit cell used in the present calculation. Color coding of the atoms: Gallium (dark green); Oxygen (red); copper (dark brown). (For interpretation of the references to color in this figure legend, the reader is referred to the web version of this article.)

$$E(V) = E_0 + \frac{9V_0B_0}{16}\left\{\left[\left(\frac{V_0}{V}\right)^{\frac{2}{3}} - 1\right]^3 B'_0 + \left[\left(\frac{V_0}{V}\right)^{\frac{3}{2}} - 1\right]^2\left[6 - 4\left(\frac{V_0}{V}\right)^{\frac{2}{3}}\right]\right\} \quad (1)$$

where symbols have their usual meaning [57–59]. After optimization, the *c*/*a* ratio has slightly increased from 3.82 to 3.83. The calculated lattice parameters, bulk modulus (B_0), and pressure derivative of bulk modules (*B*) are listed in Table 1 along with bond lengths and compared with the available theoretical results. As we could not find any experimental data for 2H-$CuGaO_2$, a comparison is made only with available theoretical data. Our calculated volume (91.31 $Å^3$) and bulk modules (142.21) are in good agreement with the available data [33,35] and bond lengths for Cu-O(Ga-O) 1.87 (2.02) are in close agreement with the theoretical values reported in Ref. [48], respectively.

3.2. Electronic properties

For an accurate description of the optical and thermoelectric properties, it is necessary to obtain a very good description of the electronic structure. To that point, we have first obtained the band structure and density of states using the TB-mbJ potential. In Fig. 2 we have plotted the band structure of 2H-$CuGaO_2$ along the high symmetry directions by taking 50 points along each segment. The VBM and CBM occurs at *H* and *Γ* points resulting in an indirect band gap, while a minimum direct band gap is observed at the *L* point. The energy band gaps computed using TB-mBJ and GGA-PBE are listed in Table 2 along with the available literature values for comparison.

Table 1
Lattice parameters (a,b,c), internal parameter (u), equilibrium volume (V), Bulk modulus (B_0), and pressure derivative of bulk modulus (B) obtained by fitting Energy vs Volume to Brich-Murnaghan equation of state (Eq. (1)), and optimized nearest neighbor distance for Cu-O and Ga-O of 2H-$CuGaO_2$.

Properties Method	lattice parameters (Å)		u	Volume (Å^3)	B_0	B	Bonds length (Å)		Refs.
	$a = b$	c					Cu_O	Ga-O	
TB-mBJ	3.019	11.562	0.090	91.31	142.2	4.30	1.869	2.016	Present work
TB-LMTO-LDA	2.973	11.595	–	88.81	175.4	–	–	–	[29]
PW91-GGA	3.025	11.560	0.085	91.59	159.6	–	–	–	[33]
PW91-GGA	3.026	11.561	–	91.73	149.4	–	–	–	[35]
LDA	2.942	11.325	0.089	84.94	–	–	–	–	[39]
GGA	3.011	11.441	0.088	89.89	–	–	–	–	
HF	2.973	11.595	0.085	88.81	192	–	1.910	1.981	[48]
HF+PW	2.913	11.455	0.087	84.24	–	–	1.864	1.957	
HF+LYP	2.931	11.340	0.086	84.42	–	–	1.867	1.957	

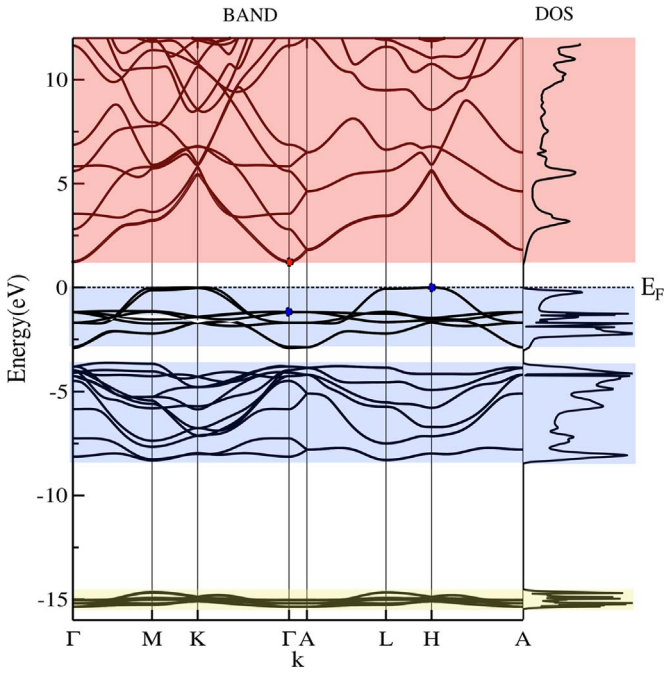

Fig. 2. Band structure of 2H-$CuGaO_2$ together with total density of states. Fermi energy (E_F) is aligned to zero for visual aid. Light blue and light red shaded regions show the valence and conduction band regions, respectively. (For interpretation of the references to color in this figure legend, the reader is referred to the web version of this article.)

Table 2
The computed direct and indirect band gap (eV) energies along with the available experimental and theoretical data for 2H-$CuGaO_2$.

	E^{dir}	E^{ind}	
PBE	2.84	0.77	Present work
TB-mBJ	3.48	1.20	”
TB-LMTO-LDA	–	0.85	[29]
PW91-GGA	–	0.77	[33]
PW91-GGA	1.48 (at Γ)	0.71	[35]
HF	11.65	–	[48]

In Fig. 2, we have plotted the band structure and total DOS using TB-mBJ. The bands in the conduction bands are highly dispersed, while valence bands show several flat bands, especially at the band edges. The bands along M-K and L-H are almost dispersion less. This indicates very high effective mass for the charge carriers at the valence band and therefore points towards p type conductivity as we shall see later. The upper valence band is separated from the lower valence band by a small gap. The higher dispersion in the lower valence band and the conduction bands are corroborated by wide peaks in the DOS plots, while the very sharp peaks in the upper valence band point towards

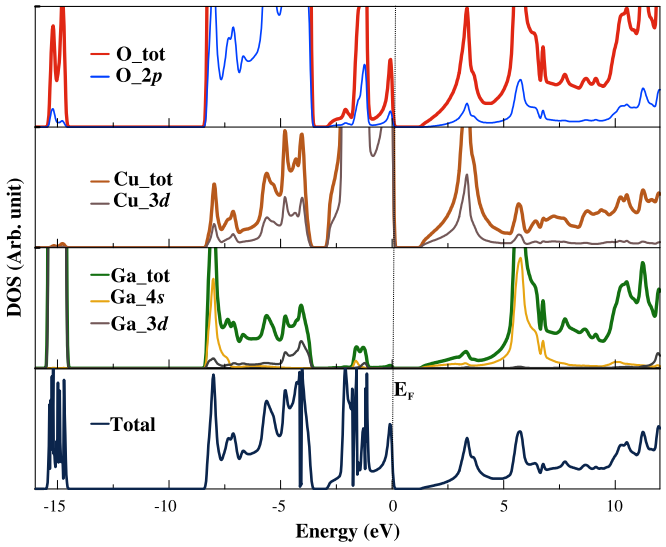

Fig. 3. Atom and orbital projected density of states. Fermi energy (E_F) is aligned to zero for visual aid.

flatness in the bands and higher concentration of the charge carriers.

For a detailed understanding of the nature of the bands and the bonding situation; in Fig. 3, we have plotted the atom and orbital projected density of states. From Fig. 3, we can see that the deep laying bands near the energy range −15 eV are contributed from Ga - 3d state with a small contribution from O - 2(s & p) state. The lower valence bands fall between the energy range −8.45 to −3.5 eV. The bands in this range have a very high contribution from O – 2p states. In the lower energy range, i.e., −8.45 eV to −7.4 eV, the O – 2p orbitals shows a higher level of mixing with Ga - 4s with a very small contribution coming from Cu - 3d state. In the interval ranging from −7.4 to −3.5 eV, Cu – 3d has a significant contribution to the bands,albeit a small contribution from Ga – 3p. The upper valence band is separated from the lower valence band by a small gap of 0.6 eV. The upper valence band is narrower compared to the lower valence band. The upper valence band has a predominant contribution from both Cu – 3d and O – 2p, while the contribution of Ga is negligible. This noticeable feature from the band structure near the VBM is an indication of a strong hybridization between Cu – 3d and O – 2p states. The hybridization reduces the ionic bonding between O – 2p state and Cu – 3d states and increases the covalent nature of the bonding between them. As a direct consequence, the covalent bonding delocalizes the bands at the top of the valence band (which is not the case in binary oxides) and therefore enhance the carrier mobility near VBM resulting in p type conductive behavior for 2H-$CuGaO_2$. Similar observations are reported by many authors [14,35]. The bands near the bottom of the conduction bands are contributed from a mixing of Cu – 3d states and O – 2p

orbitals, while the top of the lower conduction bands is derived mainly from Ga - 4*p* and O – 2*p* states with a small contribution from Cu. Unlike the valence band, the conduction band are highly dispersed, which can be directly observed from the low peaks in the DOS. The flatness in the valence bans at different energy ranges corroborates with the high peaks in DOS in the corresponding energy range.

The observed sharp peak for Cu – 3*d* (~−1.31 eV) and broader peak of O – 2*p* (~−3.5 to −5.1 eV) in Fig. 3 is very similar to the XPS and XAS spectra reported by Makhova et al. [38] for 3R-$CuGaO_2$. The slight displacement of peak can be ascribed to the small difference in their chemical environment.

3.3. Optical properties

The optical properties of the 2H-$CuGaO_2$ is obtained in terms of energy dependent dielectric constant, absorption coefficient, optical conductivity, and reflectivity. These properties were derived from the complex dielectric function,

$$\varepsilon(\omega) = \varepsilon_1(\omega) + i\varepsilon_2(\omega) \quad (2)$$

where $\varepsilon_1(\omega)$ and $\varepsilon_2(\omega)$ are real and imaginary components of the dielectric function [60]. Since the present system is hexagonal, there are two principle components i.e., directions perpendicular and parallel to the incident photons. The real and imaginary parts of dielectric constants are presented in Fig. 4(a) and (b), respectively.

The prominent peaks in imaginary component of dielectric tensor at ~4.1 and 4.7 eV arise due to absorptive transitions from the valence bands to the conduction bands. The imaginary part of the dielectric component is dominated by a broader peak originating from 3.1 eV and attaining an intense peak at ~4.1 eV. This energy range is of our particular interest, since the intensity of UV light falls rapidly beyond this energy window. Since the optical band gap (direct) of 2H-$CuGaO_2$ falls in this range, the broadened peak can be ascribed to the transitions between flat dispersion contribution of the topmost VB and lowest CB at the k point *L*. The average high-frequency dielectric constants (ε^{∞}; $0 \le \hbar\omega \le E_g$) obtained using PBE and mBJ are 5.02 and 3.42, respectively.

The decreasing trend in $\varepsilon_2(\omega)$ is consistent with the increasing trend for the band gap (Table 2), which is in accordance with the Penn relation [61],

$$\varepsilon_1(0) \approx 1 + (\hbar\omega_p/\Delta E_g)^2 \quad (3)$$

Frequency dependent absorption coefficient of 2H-$CuGaO_2$ is shown in Fig. 5. For the present case, a broad peak starts at ~3.1 eV and attains a sharp peak at 4.2 eV with maximum absorption coefficient of 97×10^4 cm^{-1}. For the photons having high energies the deep electronic states (i.e. bands lying at the lower valence band), also get involved in the interaction and hence for the formation of peaks in the higher energy range, the full band structure plays a vital role,which is beyond the scope of present study.

Fig. 6 shows the refractive index of $CuGaO_2$. The average static refractive index obtained is 1.84. It is apparent from Fig. 6 that the values of n(ω) increases as the photon energy increases and reaches its maximum value 3.49 at 3.147 eV. Beyond this energy, the refractive index starts to decrease up to 0.77 at 5.24 eV. In the inset of Fig. 6 we illustrated the birefringence (the difference between propagation speed of extraordinary ($n^{\parallel}(\omega)$)) and ordinary rays ($n^{\perp}(\omega)$) which predict the nearly isotropic nature of 2H-$CuGaO_2$ up to ~2.0 eV which falls in the visible region of solar spectrum. After this energy range it is behaving as an anisotropic medium for the incident light and near the energy range 5.26 eV the system is perfectly anisotropic. The positive value of the refractive index in the shown energy range revels the linearity of 2H-$CuGaO_2$ to the electromagnetic frequency.

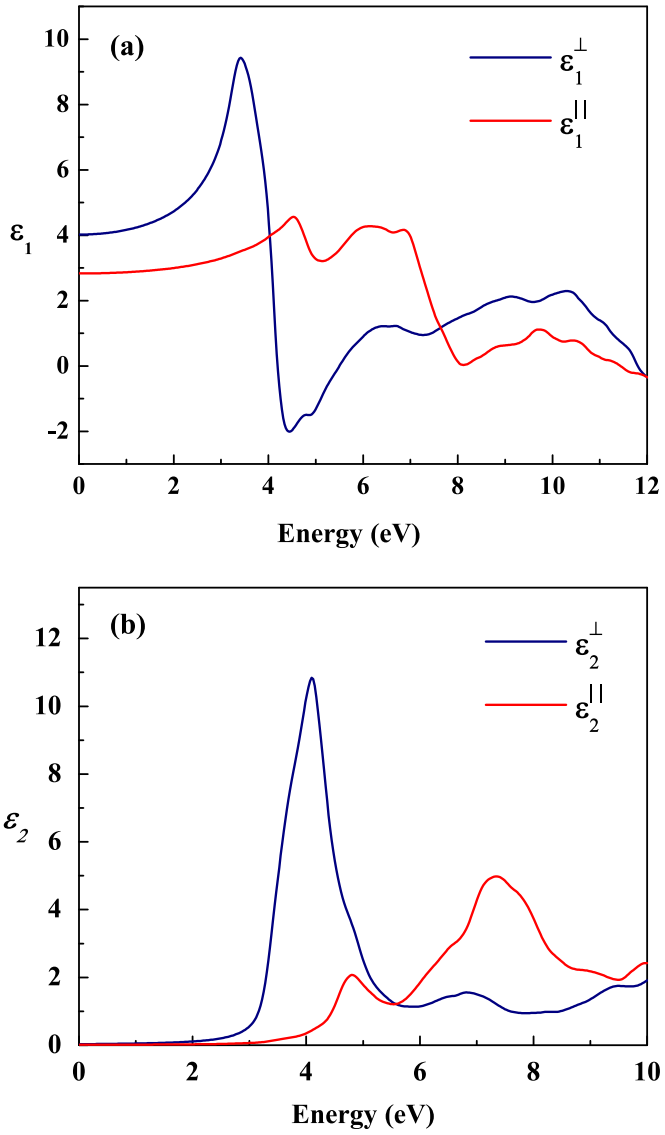

Fig. 4. Calculated (a) real component (upper panel), and (b) imaginary component (bottom panel) of complex dielectric function of 2H-$CuGaO_2$. Blue and red lined shows the perpendicular and parallel directions to the incident photon. (For interpretation of the references to color in this figure legend, the reader is referred to the web version of this article.)

3.4. Thermoelectric properties

The electronic transport coefficients for the present compound was evaluated by using post DFT treatment involving the semi-classical Boltzmann and the rigid band model. Boltztrap code is a well reliable tool to calculate the electronic transport properties of thermoelectric materials [54–56]. To solve the semi-classical Boltzmann equations to get the conductivity tensor and other transport coefficients, the code requires a smooth analytical representation of bands. This was obtained by using Fourier expansion of the band energies using symmetry-conserving star functions. In BoltzTraP, a constant value for relaxation time (τ) is assumed, typically around 10^{-14} s, so that one can get electrical conductivity per relaxation time (S/τ).

We here focus on electrical conductivity (S/τ), Seebeck coefficient (S), electronic thermal conductivity (k_e), and the electronic power factor ($P = S^2\sigma$) as a function of chemical potential and are reported in the region ± 0.195 (μ-E_F) eV at constant temperature of 300–800 K. The thermoelectric efficiency of a thermoelectric material is expressed by the figure of merit (ZT), where

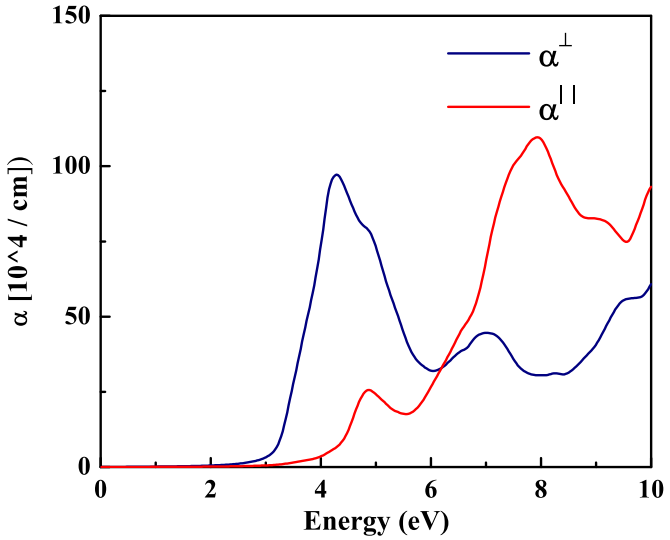

Fig. 5. Calculated absorption coefficient of 2H-$CuGaO_2$. Blue and red lined shows the perpendicular and parallel directions to the incident photon. (For interpretation of the references to color in this figure legend, the reader is referred to the web version of this article.)

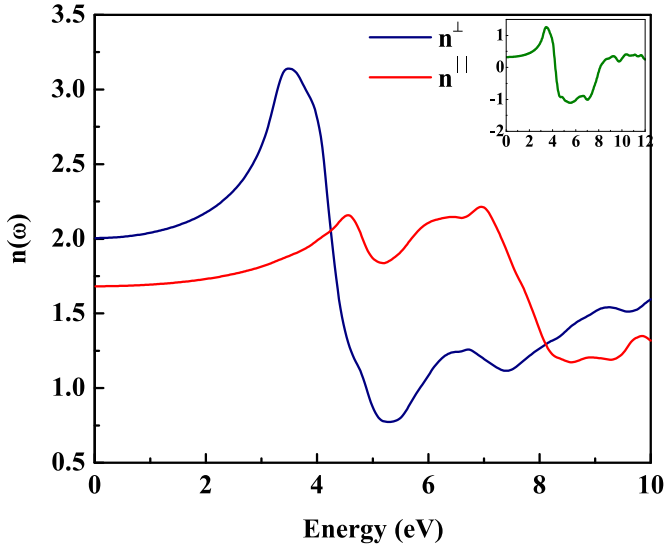

Fig. 6. Calculated refractive index. Blue and red lines show the perpendicular and parallel directions to the incident photon. The figure in the inset shows birefringence.

$$ZT = \sigma S^2 T/(\kappa_{el} + \kappa_{ph}) \quad (4)$$

wherein, σ-electrical conductivity, S-Seebeck coefficient, T-temperature, κ_{el} the electronic thermal conductivity per relaxation time, and κ_{ph} the phonon thermal conductivity per relaxation time. So, a material having high electrical conductivity, large Seebeck coefficient and low thermal conductivity show high thermoelectric efficiency. However, lack of available experimental data for 2H-$CuGaO_2$ make it difficult for a quantitative comparison.

The calculated electrical conductivity as a function of chemical potential is illustrated in Fig. 7 for perpendicular (⊥) and parallel (‖) polarization of the incident photon at 300–800 K. As the electronic distribution near the Fermi level contributes significantly to the materials properties and directly get affected with any external treatments. So, for higher temperature, the electrical conductivity will be high near the (μ-E_F) because of enhancing the charge carrier's concentration and the mobility of the electrons and holes in the conduction and valence band. When the temperature is increased, they go through a lattice scattering and thus shows the reduced value of

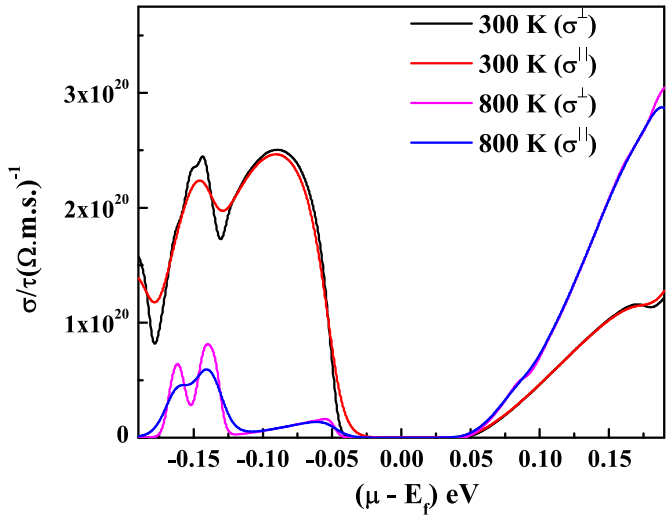

Fig. 7. Electrical conductivity per relaxation time as a function of chemical potential ($\mu - E_F$) eV for temperatures 300 and 800 K for the parallel and perpendicular components of the incident photon.

Table 3
The highest value of electrical conductivity for $CuGaO_2$ in the chemical potentials region of ± 0.055 (μ-E_F) eV.

Temp (K)	*p*-type		*n*-type	
	(⊥)	(‖)	(⊥)	(‖)
300	4.30E + 13	4.52E + 17	1.06E + 13	7.31E + 16
800	6.10E + 11	1.24E + 16	9.28E + 11	1.91E + 16

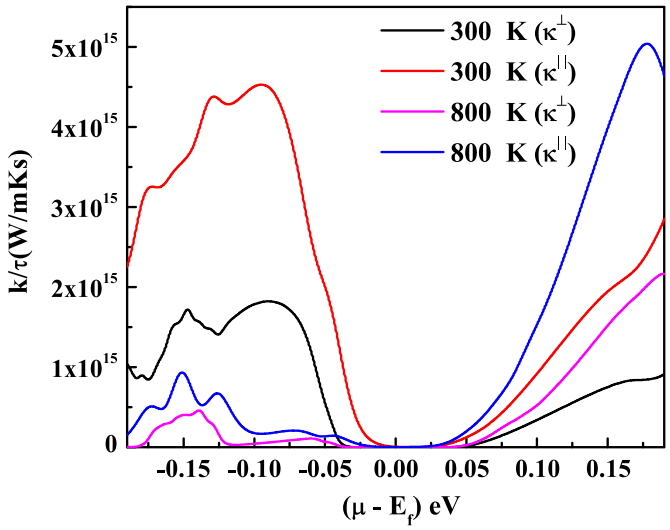

Fig. 8. Electronic thermal conductivity per relaxation time as a function of chemical potential (μ-E_F) eV for temperatures 300 and 800 K for the parallel and perpendicular components of the incident photon.

electrical conductivity. We can see that both the polarized components of electrical conductivity for incident photon show a considerable difference which could attribute to the anisotropic nature of $CuGaO_2$. The maximum value of electrical conductivity in the chemical potential range of ± 0.055 (μ-E_F) eV is reported in Table 3. A similar trend for electrical conductivity is reported by many authors [54–56].

In Fig. 8, we depicted electronic thermal conductivity as a function of chemical potential (μ-E_F) eV. We should consider here that the thermal conductivity has contributions from the lattice vibrations (phonon contribution) and electronic excitations (electronic contribu-

Table 4
Electronic thermal conductivity for $CuGaO_2$ in the chemical potential region of ± 0.055 (μ-E_F) eV for temperatures 300 and 800 K for the parallel and perpendicular components of the incident photon.

Temp (K)	*p*-type		*n*-type	
	(⊥)	(∥)	(⊥)	(∥)
300	2.27E + 10	1.29E + 14	5.34E + 09	1.78E + 13
800	3.52E + 08	5.85E + 12	5.37E + 08	6.83E + 12

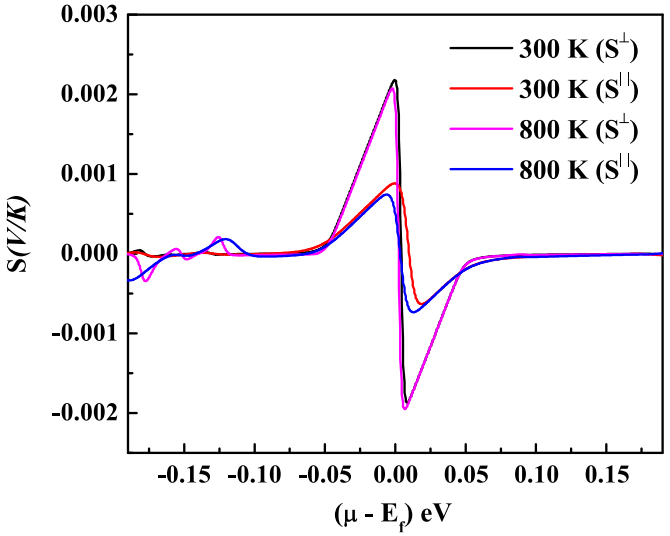

Fig. 9. The Seeback coefficient as a function of chemical potential (μ-E_F) eV for temperatures 300 and 800 K for the parallel and perpendicular components of the incident photon.

tion) but the BoltzTraP calculates only the electronic part [54–56]. For the chemical potential ranges ± 0.055 (μ-E_F) eV, the electronic thermal conductivity is minimum and therefore the $CuGaO_2$ can give its maximum efficiency. The maximum value of electronic thermal conductivity for the p-/n-type region for $CuGaO_2$ is listed in Table 4. We can predict from the table that for the chemical potential range ± 0.055 (μ-E_F) the electronic thermal conductivity is lowest and thus the therm power shall be maximum in this range. For p-type region the perpendicular component is dominating factor while for n-type region parallel component is higher than perpendicular.

The temperature dependent Seebeck coefficient (S) for the compound of the present investigation is shown in Fig. 9. The Seebeck coefficient represents the ratio of the voltage difference to the temperature difference. With increasing temperature, a temperature gradient is generated resulting one side of the material hotter than the other side. The energetic distribution of the free charge carriers is shifted to higher energy states upon heating which leads to a displacement diffusion current towards the cold side. Depending upon the nature of charge carriers the magnitude of Seebeck coefficient may be positive or negative. From Fig. 9, we see that the resultant magnitude is larger for p-type character and hence making $CuGaO_2$ a p-type semiconductor. The Seebeck coefficient shows two dominating peaks near the Fermi level (-E_F). In the p-/n-type region, it is located at ± 0.02 (μ-E_F) eV. The highest values for p-/n-type region of Seebeck coefficient are listed in Table 5.

For higher value of temperature, Seebeck coefficient decreases and perpendicular component is higher in magnitude. In the range between these two critical points this material exhibits excellent thermoelectric properties. Beyond these critical points Seebeck coefficient vanishes, and material is not useful for thermoelectric properties. In Figs. 10 and 11, we have plotted the power factor and figure of merit for $CuGaO_2$,

Table 5
Seebeck Coefficient for $CuGaO_2$ in Vμ/K for ± 0.055 (μ-E_F) eV in the different regions of the chemical potential.

Temp (K)	*p*-type		*n*-type	
	(⊥)	(∥)	(⊥)	(∥)
300	2.18E + 03	8.84E + 02	2.17E + 03	8.82E + 02
800	2.07E + 03	7.43E + 02	1.76E + 03	4.73E + 02

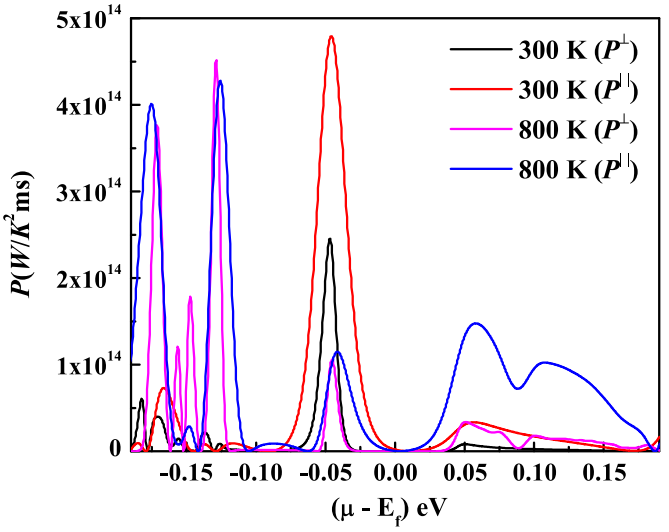

Fig. 10. Power factor for $CuGaO_2$ as a function of chemical potential (μ-E_F) eV for temperatures 300 and 800 K for the parallel and perpendicular components of the incident photon.

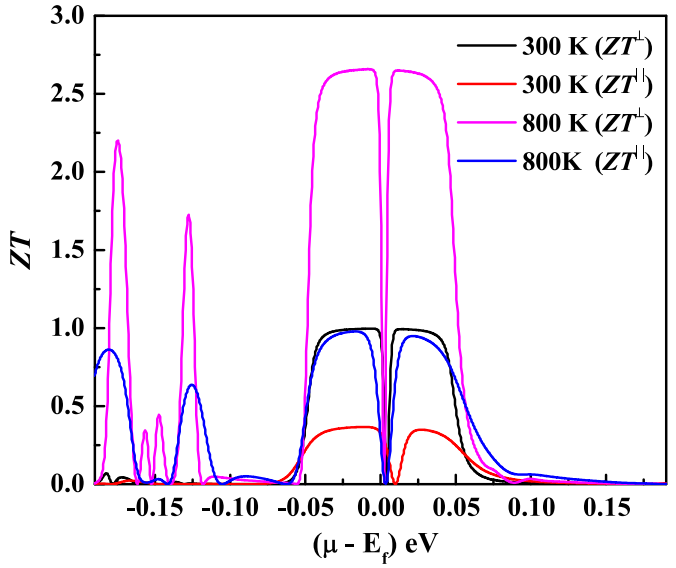

Fig. 11. Figure of merit for $CuGaO_2$ as a function of chemical potential (μ-E_F) eV for temperatures 300 and 800 K for the parallel and perpendicular components of the incident photon.

respectively and Tables 6, 7 depicts the maximum value of power factor and figure of merit, respectively.

We see that in the chemical potential range ± 0.055 (μ-E_F) eV, there are two pronounced sharp peaks in power factor plot while in the figure of merit we see the minimum value of it. The figure or merit shows its maximum value in the chemical potential range ± 0.055 (μ-E_F) eV and beyond this limit, it decreases. This trend is expected because Seebeck coefficient is dominating factor for this range. The power factor comes

Table 6
The peaks position of the power factor for $CuGaO_2$ in (W/K^2 ms) in the different regions of the chemical potential in the range of ± 0.055 (μ-E_F) eV.

Temp (K)	*p*-type		*n*-type	
	(⊥)	(‖)	(⊥)	(‖)
300	2.45E + 14	4.79E + 14	1.05E + 14	1.15E + 14
800	8.11E + 12	3.34E + 13	3.37E + 13	1.48E + 14

Table 7
Figure of Merit (ZT) for $CuGaO_2$. The first higher peak for both p and n type regions are reported here which are originated around ± 0.055 (μ-E_F) eV for parallel components in the different regions of the chemical potential.

Temp (K)	*p*-type		*n*-type	
	(⊥)	(‖)	(⊥)	(‖)
300	0.99	0.366	2.66	0.97
800	0.99	0.34	2.65	0.95

in the numerator of the figure of merit but the electronic thermal conductivity occurs in the denominator. Near the Fermi energy, electronic thermal conductivity is minimum which is responsible for the lowest value of power factor. The highest value of power factor occurs for 800 K and then it decreases with decreasing the temperature.

In the literature, it is confidently argued that the thermoelectric power S is closely related to the chemical potential (μ) [62]. At absolute temperature, chemical potential coincides with the Fermi level and hence it is referenced at the top of the valence band. As temperature increases the chemical potential falls within the VBM and CBM. Therefore, from the linear response theory, temperature dependence of chemical potential increases the Seebeck coefficient (thermoelectric power) which is directly proportional to the absolute temperature [62]. From Table 5, we see that the magnitude of p-type component in perpendicular and parallel components are high in comparison to the respective component of the n-type character. At low temperature, the magnitude of the p- and n- type components are the same whereas with the increase in temperature (800 K) there is a significant difference between both components, wherein p-type components are dominating. According to Eq. (4), ZT is directly proportional to the square of the Seebeck coefficient. Therefore, at higher temperature, this material will show excellent thermoelectric properties.

4. Conclusions

In summary, we have obtained an accurate description of the electronic structure and optical properties of $CuGaO_2$ using TB-mBJ exchange potential within the first-principles calculations. The obtained band gap is indirect having the value of 1.20 eV. Specifically, the band structure is explained in terms of density of states. Our further study reveals that these notable improvements are achieved because mBJ potential describes accurately the energy levels of Cu - 3d states and the hybridization between the orbitals.

We found some variation with the results reported by Liu et al. and with that of reported by Dixit et al. and this is due to consideration of different types of functional and potentials (mBJ).

The first peak in the perpendicular component of dielectric function is near the visible region which shows that $CuGaO_2$ also may be a useful material for transparent electronics. The thermoelectric properties were studied as a function of chemical potential and are reported in the range of ± 0.195 (μ-E_F) eV at constant temperature 300 and 800 K. The investigated thermoelectric properties predict the usefulness of $CuGaO_2$ for thermoelectric technological applications in the higher temperature range near the Fermi energy level. Our thermoelectric investigations reveals the p-type semiconductive nature of the present compound which is in agreement with the available information in the literature. Conclusively, the $CuGaO_2$ in H- phase may also be useful of transparent electronic devices. It is expected to give maximum efficiency at high temperature at the chemical potential range near the Fermi energy level.

Acknowledgments

Authors are grateful to Prof. Blaha and his team for the support with WIEN2k code. KCB is thankful to UGC, New-Delhi, India for providing financial support in the form of Dr. D.S. Kothari Post-doctoral Fellowship wide letter number PH/13-14/0113. The authors gratefully acknowledge IUAC, New Delhi for providing computing facilities.

References

[1] H. Kawazoe, M. Yasukawa, H. Hyodo, M. Kurita, H. Yanagi, H. Hosono, A high-yield hydrothermal preparation of $CuAlO_2$, Nature 389 (1997) 939–942. http://dx.doi.org/10.1038/40087.
[2] M. Kumar, H. Zhao, C. Persson, Study of band-structure, optical properties and native defects in $A^{I}B^{III}O_2$ (A^{I} = Cu or Ag, B^{III} = Al, Ga or In) delafossites, Semicond. Sci. Technol. 28 (6) (2013) 065003. http://dx.doi.org/10.1088/0268-1242/28/6/065003 (1)(–10).
[3] H. Yanagi, S.-i. Inoue, K. Ueda, H. Kawazoe, H. Hosono, N. Hamada, Electronic structure and optoelectronic properties of transparent p-type conducting $CuAlO_2$, J. Appl. Phys. 88 (7) (2000) 4159–4163. http://dx.doi.org/10.1063/1.1308103.
[4] Z. Deng, X. Zhu, R. Tao, W. Dong, X. Fang, Synthesis of $CuAlO_2$ ceramics using sol-gel, Mater. Lett. 61 (3) (2007) 686–689. http://dx.doi.org/10.1016/j.matlet.2006.05.042.
[5] W.C. Sheets, E.S. Stampler, M.I. Bertoni, M. Sasaki, T.J. Marks, T.O. Mason, K.R. Poeppelmeier, Silver delafossite oxides, Inorg. Chem. 47 (7) (2008) 2696–2705. http://dx.doi.org/10.1021/ic702197h.
[6] A. Banerjee, K. Chattopadhyay, Recent developments in the emerging field of crystalline p-type transparent conducting oxide thin films, Prog. Cryst. Growth Charact. Mater. 50 (1–3) (2005) 52–105. http://dx.doi.org/10.1016/j.pcrysgrow.2005.10.001.
[7] J.R. Smith, T.H. Van Steenkiste, X.G. Wang, Thermal photocatalytic generation of H_2 over $CuAlO_2$ nanoparticle catalysts in H_2O, Phys. Rev. B 79 (4) (2009) 2–5. http://dx.doi.org/10.1103/PhysRevB.79.041403.
[8] H. Dixit, R. Saniz, S. Cottenier, D. Lamoen, B. Partoens, Electronic structure of transparent oxides with the Tran-Blaha modified Becke-Johnson potential, J. Phys. Condens. Matter 24 (20) (2012) 205503. http://dx.doi.org/10.1088/0953-8984/24/20/205503 (1)(-9).
[9] T. Minami, Transparent conducting oxide semiconductors for transparent electrodes, Semicond. Sci. Technol. 20 (4) (2005) S35–S44. http://dx.doi.org/10.1088/0268-1242/20/4/004.
[10] D. Segev, S.-H. Wei, Structure-derived electronic and optical properties of transparent conducting oxides, Phys. Rev. B 71 (12) (2005) 125129. http://dx.doi.org/10.1103/PhysRevB.71.125129 (1)(-11).
[11] M.A. Ali, A. Khan, S.H. Khan, T. Ouahrani, G. Murtaza, R. Khenata, S.B. Omran, First principles study of Cu based Delafossite Transparent Conducting Oxides $CuXO_2$ (X=Al, Ga, In, B, La, Sc, Y), Mater. Sci. Semicond. Process. 38 (2015) 57–66 (⟨http://dx.doi.org/10.1016/j.mssp.2015.03.038⟩).
[12] Z. Zang, A. Nakamura, J. Temmyo, Single cuprous oxide films synthesized by radical oxidation at low temperature for pv application, Opt. Express 21 (9) (2013) 11448–11456. http://dx.doi.org/10.1364/OE.21.011448 ⟨http://www.opticsexpress.org/abstract.cfm?URI=oe-21-9-11448⟩.
[13] Z. Zang, X. Zeng, J. Du, M. Wang, X. Tang, Femtosecond laser direct writing of microholes on roughened zno for output power enhancement of ingan light-emitting diodes, Opt. Lett. 41 (15) (2016) 3463–3466. http://dx.doi.org/10.1364/OL.41.003463 ⟨http://ol.osa.org/abstract.cfm?URI=ol-41-15-3463⟩.
[14] M.N. Huda, Y. Yan, A. Walsh, S.-H. Wei, M.M. Al-Jassim, Group-IIIA versus IIIB delafossites: electronic structure study, Phys. Rev. B 80 (2009). http://dx.doi.org/10.1103/PhysRevB.80.035205 (035205)(1)(-7).
[15] M. Kumar, C. Persson, Structural, electronic and optical properties of silver delafossite oxides: a first-principles study with hybrid functional, Phys. B Condens. Matter 422 (2013) 20–27. http://dx.doi.org/10.1016/j.physb.2013.04.035.
[16] R. Gillen, J. Robertson, Band structure calculations of $CuAlO_2$, $CuGaO_2$, $CuInO_2$, and $CuCrO_2$ by screened exchange, Phys. Rev. B 84 (2011). http://dx.doi.org/10.1103/PhysRevB.84.035125 (035125)(1)(-7).
[17] M. Lee, D. Kim, Y.T. Yoon, Y.I. Kim, Photoelectrochemical water splitting on a delafossite $CuGaO_2$ semiconductor electrode, Bull. Korean Chem. Soc. 35 (11) (2014) 3261–3266. http://dx.doi.org/10.5012/bkcs.2014.35.11.3261.
[18] K. Ueda, T. Hase, H. Yanagi, H. Kawazoe, H. Hosono, H. Ohta, M. Orita, M. Hirano, Epitaxial growth of transparent p-type conducting $CuGaO_2$ thin films on sapphire (001) substrates by pulsed laser deposition, J. Appl. Phys. 89 (3) (2001) 1790–1793. http://dx.doi.org/10.1063/1.1337587.
[19] C. Granqvist, A. HultÅker, Transparent and conducting ITO films: new develop-

ments and applications, Thin Solid Films 411 (1) (2002) 1–5. http://dx.doi.org/10.1016/S0040-6090(02)00163-3.
[20] I. Hamberg, C.G. Granqvist, Evaporated Sn-doped In_2O_3 films: basic optical properties and applications to energy-efficient windows, J. Appl. Phys. 60 (11) (1986) R123–R157. http://dx.doi.org/10.1063/1.337534.
[21] A. Banerjee, R. Maity, K. Chattopadhyay, Preparation of p-type transparent conducting $CuAlO_2$ thin films by reactive DC sputtering, Mater. Lett. 58 (1–2) (2004) 10–13 ⟨http://dx.doi.org/10.1016/S0167-577X)(03)00395-1⟩..
[22] S. Gao, Y. Zhao, P. Gou, N. Chen, Y. Xie, Preparation of $CuAlO_2$ nanocrystalline transparent thin films with high conductivity, Nanotechnology 14 (5) (2003) 538–541. http://dx.doi.org/10.1088/0957-4484/14/5/310.
[23] S. Götzendörfer, C. Polenzky, S. Ulrich, P. Löbmann, Preparation of $CuAlO_2$ and $CuCrO_2$ thin films by sol-gel processing, Thin Solid Films 518 (4) (2009) 1153–1156. http://dx.doi.org/10.1016/j.tsf.2009.02.153.
[24] B.J. Ingram, G.B. González, T.O. Mason, D.Y. Shahriari, A. Barnabè, D. Ko, K.R. Poeppelmeier, Transport and defect mechanisms in cuprous delafossites. 1. Comparison of hydrothermal and standard solid-state synthesis in $CuAlO_2$, Chem. Mater. 16 (26) (2004) 5616–5622. http://dx.doi.org/10.1021/cm048983c.
[25] D.Y. Shahriari, A. Barnabè, T.O. Mason, K.R. Poeppelmeier, A. High-Yield, Hydrothermal preparation of $CuAlO_2$, Inorg. Chem. 40 (23) (2001) 5734–5735. http://dx.doi.org/10.1021/ic015556h.
[26] X. Nie, S.-H. Wei, S.B. Zhang, Bipolar doping and band-gap anomalies in delafossite transparent conductive oxides, Phys. Rev. Lett. 88 (2002). http://dx.doi.org/10.1103/PhysRevLett.88.066405 (066405)(1)(-4).
[27] J. Vidal, F. Trani, F. Bruneval, M.A.L. Marques, S. Botti, Effects of electronic and lattice polarization on the band structure of delafossite transparent conductive oxides, Phys. Rev. Lett. 104 (13) (2010) 1–4. http://dx.doi.org/10.1103/PhysRevLett.104.136401.
[28] J. Pellicer-Porres, A. Segura, A.S. Gilliland, A. Munöz, P. Rodríguez-Hernández, D. Kim, M.S. Lee, T.Y. Kim, On the band gap of $CuAlO_2$ delafossite, Appl. Phys. Lett. 88 (18) (2006). http://dx.doi.org/10.1063/1.2200398 (181904)(1)(-3).
[29] V. Jayalakshmi, R. Murugan, B. Palanivel, Electronic and structural properties of $CuMO_2$ (M = Al, Ga, In), J. Alloy. Compd. 388 (1) (2005) 19–22. http://dx.doi.org/10.1016/j.jallcom.2004.07.009.
[30] L. Zhang, L. McMillon, J. McNatt, Gas-dependent bandgap and electrical conductivity of Cu_2O thin films, Sol. Energy Mater. Sol. Cells 108 (2013) 230–234 ⟨http://dx.doi.org/10.1016/j.solmat.2012.05.010⟩..
[31] M. Yu, G. Natu, Z. Ji, Y. Wu, p-Type dye-sensitized solar cells based on delafossite $CuGaO_2$ nanoplates with saturation photovoltages exceeding 460 mV, J. Phys. Chem. Lett. 3 (9) (2012) 1074–1078. http://dx.doi.org/10.1021/jz3003603.
[32] A. Renaud, B. Chavillon, L. Le Pleux, Y. Pellegrin, E. Blart, M. Boujtita, T. Pauporte, L. Cario, S. Jobic, F. Odobel, $CuGaO_2$: a promising alternative for NiO in p-type dye solar cells, J. Mater. Chem. 22 (2012) 14353–14356. http://dx.doi.org/10.1039/C2JM31908J.
[33] W.T. Liu, Z.T. Liu, First-principles study on the elastic and electronic properties of 2H-$CuGaO_2$, Appl. Mech. Mater. 446–447 (2013) 3–7 (⟨doi:10.4028/www.scientific.net/AMM.446-447.3⟩.).
[34] R.B. Gall, N. Ashmore, M.A. Marquardt, X. Tan, D.P. Cann, Synthesis, microstructure, and electrical properties of the delafossite compound cugao$_2$, J. Alloy. Compd. 391 (1–2) (2005) 262–266 ⟨http://dx.doi.org/10.1016/j.jallcom.2004.08.070⟩..
[35] Q.-J. Liu, Z.-T. Liu, L.-P. Feng, H. Tian, First-principles study of structural, elastic, electronic, and optical properties of γ-TeO_2, Phys. B Condens. Matter 405 (15) (2010) 3159–3163 ⟨http://dx.doi.org/10.1016/j.physb.2010.04.034⟩..
[36] M.C. Nguyen, X. Zhao, C.-Z. Wang, K.-M. Ho, First-principles study of direct and narrow band gap semiconducting β-$CuGaO_2$, Mater. Res. Express 2 (4) (2015). http://dx.doi.org/10.1088/2053-1591/2/4/045902 (045902)(1)(-6).
[37] M.F. Iozzi, P. Vajeeston, R. Vidya, P. Ravindran, H. Fjellvag, Structural and electronic properties of transparent conducting delafossite: a comparison between the $AgBO_2$ and $CuBO_2$ families (B = Al,Ga, In and Sc, Y), RSC Adv. 5 (2) (2015) 1366–1377. http://dx.doi.org/10.1039/C3RA47531J.
[38] L. Makhova, D. Wett, M. Lorenz, I. Konovalov, X-ray spectroscopic investigation of forbidden direct transitions in $CuGaO_2$ and $CuInO_2$, Phys. Status Solidi Appl. Mater. Sci. 203 (11) (2006) 2861–2866. http://dx.doi.org/10.1002/pssa.200669634.
[39] H.C. Kandpal, R. Seshadri, First-principles electronic structure of the delafossites ABO_2 (A = Cu, Ag, Au; B = Al, Ga, Sc, In, Y): evolution of d^{10}-d^{10} interactions, Solid State Sci. 4 (2002) 1045–1052. http://dx.doi.org/10.1016/S1293-2558(02)01363-8.
[40] T.I. Draskovic, M. Yu, Y. Wu, 2H-$CuScO_2$ prepared by low-temperature hydrothermal methods and post-annealing effects on optical and photoelectrochemical properties, Inorg. Chem. 54 (11) (2015) 5519–5526. http://dx.doi.org/10.1021/acs.inorgchem.5b00575.
[41] T. Omata, H. Nagatani, I. Suzuki, M. Kita, H. Yanagi, N. Ohashi, Wurtzite $CuGaO_2$: a new direct and narrow band gap oxide semiconductor applicable as a solar cell absorber, J. Am. Chem. Soc. 136 (9) (2014) 3378–3381. http://dx.doi.org/10.1021/ja501614n.
[42] D.O. Scanlon, A. Walsh, Polymorph engineering of $CuMO_2$ (M = Al, Ga, Sc, Y) semiconductors for solar energy applications: from delafossite to wurtzite, Acta Crystallogr. Sect. B: Struct. Sci. 71 (6) (2015) 702–706. http://dx.doi.org/10.1107/S2052520615018387.
[43] F. Trani, J. Vidal, S. Botti, M.A.L. Marques, Band structures of delafossite transparent conductive oxides from a self-consistent *GW* approach, Phys. Rev. B 82 (2010). http://dx.doi.org/10.1103/PhysRevB.82.085115 (085115)(1)(-11).
[44] I. Suzuki, H. Nagatani, M. Kita, Y. Iguchi, C. Sato, H. Yanagi, N. Ohashi, T. Omata, First principles calculations of ternary wurtzite β-$CuGaO_2$, J. Appl. Phys. 119 (9) (2016). http://dx.doi.org/10.1063/1.4942619 (095701)(1)(-7).
[45] L.-J. Shi, Z.-J. Fang, J. Li, First-principles study of p-type transparent conductive oxides $CuXO_2$ (X=Y, Sc, and Al), J. Appl. Phys. 104 (7) (2008). http://dx.doi.org/10.1063/1.2991157 (073527)(1)(-5).
[46] I. Herraiz-Cardona, F. Fabregat-Santiago, A. Renaud, B. Julián-Lèpez, F. Odobel, L. Cario, S. Jobic, S. Gimènez, Hole conductivity and acceptor density of p-type $CuGaO_2$ nanoparticles determined by impedance spectroscopy: the effect of Mg doping, Electrochim. Acta 113 (2013) 570–574 ⟨http://dx.doi.org/10.1016/j.electacta.2013.09.129⟩..
[47] J. Tate, M. Jayaraj, A. Draeseke, T. Ulbrich, A. Sleight, K. Vanaja, R. Nagarajan, J. Wager, R. Hoffman, p-type oxides for use in transparent diodes, Thin Solid Films 411 (1) (2002) 119–124 ⟨http://dx.doi.org/10.1016/S0040-6090)(02)00199-2⟩..
[48] A. Buljan, P. Alemany, E. Ruiz, Electronic structure and bonding in $CuMO_2$ (M = Al, Ga, Y) delafossite-type oxides: an Ab initio study, J. Phys. Chem. B 103 (38) (1999) 8060–8066. http://dx.doi.org/10.1021/jp984420a.
[49] K.C. Bhamu, K.R. Priolkar, Electronic and optical properties of $AgAlO_2$: a first-principles study, Mater. Chem. Phys. 190 (2017) 114–119. http://dx.doi.org/10.1016/j.matchemphys.2016.12.069.
[50] K.C. Bhamu, R. Khenata, S.A. Khan, M. Singh, K.R. Priolkar, Electronic, optical and thermoelectric properties of 2H-$CuAlO_2$: a first principles study, J. Electron. Mater. 45 (1) (2016) 615–623. http://dx.doi.org/10.1007/s11664-015-4160-3.
[51] F. Tran, P. Blaha, Accurate band gaps of semiconductors and insulators with a semilocal exchange-correlation potential, Phys. Rev. Lett. 102 (22) (2009) 5–8. http://dx.doi.org/10.1103/PhysRevLett.102.226401.
[52] P. Blaha, K. Schwarz, G. Madsen, D. Kvasnicka, J. Luitz, WIEN2k, An Augmented Plane Wave Plus Local Orbitals Program for Calculating Crystal Properties, Vienna University of Technology, 2016.
[53] J.P. Perdew, K. Burke, M. Ernzerhof, Generalized gradient approximation made simple, Phys. Rev. Lett. 77 (1996) 3865–3868. http://dx.doi.org/10.1103/PhysRevLett.77.3865.
[54] G.K.H. Madsen, D.J. Singh, BoltzTraP. A code for calculating band-structure dependent quantities, Comput. Phys. Commun. 175 (1) (2006) 67–71. http://dx.doi.org/10.1016/j.cpc.2006.03.007.
[55] A.H. Reshak, S. Auluck, Thermoelectric properties of Nowotny-Juza NaZnX (X = P, As and Sb) compounds, Comput. Mater. Sci. 96 (PA) (2015) 90–95. http://dx.doi.org/10.1016/j.commatsci.2014.09.008.
[56] A.H. Reshak, S.A. Khan, S. Auluck, Thermoelectric properties of a single graphene sheet and its derivatives, J. Mater. Chem. C 2 (13) (2014) 2346–2352. http://dx.doi.org/10.1039/c3tc32260b.
[57] F. Birch, Finite elastic strain of cubic crystals, Phys. Rev. 71 (1947) 809–824. http://dx.doi.org/10.1103/PhysRev.71.809.
[58] J.R. Macdonald, Review of some experimental and analytical equations of state, Rev. Mod. Phys. 41 (1969) 316–349. http://dx.doi.org/10.1103/RevModPhys.41.316.
[59] F.D. Murnaghan, The compressibility of media under extreme pressures, Proc. Natl. Acad. Sci. 30 (9) (1944) 244–247. http://dx.doi.org/10.1073/pnas.30.9.244.
[60] C. Ambrosch-Draxl, J.O. Sofo, Linear optical properties of solids within the full-potential linearized augmented planewave method, Comput. Phys. Commun. 175 (1) (2006) 1–14. http://dx.doi.org/10.1016/j.cpc.2006.03.005.
[61] D.R. Penn, Wave-number-dependent dielectric function of semiconductors, Phys. Rev. 128 (5) (1962) 2093–2097. http://dx.doi.org/10.1103/PhysRev.128.2093.
[62] A. Yamamoto, K. Ogawa, T. Takeuchi, Effect of chemical potential on thermoelectric power of biisub¿2i/sub¿teisub¿3i/sub¿ and biisub¿2i/sub¿sei sub¿3i/sub¿, Mater. Trans. 52 (8) (2011) 1539–1545. http://dx.doi.org/10.2320/matertrans.E-M2011809.